

Nonlocal Effects on Surface Plasmon Polariton Propagation in Graphene Nanoribbons

Giampiero Lovat, *Member, IEEE*, Rodolfo Araneo, *Senior Member, IEEE*, Paolo Burghignoli, *Senior Member, IEEE*, and George W. Hanson, *Fellow, IEEE*

Abstract—Fundamental properties of surface plasmon polariton modes propagating along graphene nanoribbons are investigated by means of a full-wave method-of-moments approach adopting a spatially dispersive dyadic model for graphene conductivity. Modal propagation, current profiles, field distributions, and characteristic impedances are studied in detail showing the dramatic effects of spatial dispersion and the need to go beyond the usual weak (low- q) spatial dispersion formulation.

Index Terms—Graphene, nanoribbons, surface plasmon polariton.

I. INTRODUCTION

PLANAR electromagnetic structures incorporating graphene layers have received considerable attention in the last few years for waveguide, antenna, and shielding applications. In particular, graphene nanoribbons (GNRs) have been proposed in various configurations, as possible interconnects in integrated circuits [1]–[3]. GNRs, either free-standing or placed in a stratified dielectric structure, support a variety of propagation modes, including surface-plasmon modes [4], [5]. Surface plasmon polariton (SPP) propagation in graphene nanostructures has recently attracted interest for the possibility of strong confinement of electromagnetic energy at subwavelength scales, tuned and controlled by a gate voltage or through chemical doping. Other applications of graphene plasmons include optical signal processing, light modulation, sensing, spectral photometry, quantum optics, and nonlinear photonics [6], [7].

Here, we aim at studying the fundamental properties of the dominant SPP mode supported by a monolayer GNR placed on top of a dielectric substrate, employing a rigorous full-wave non-Galerkin method-of-moments (MoM) approach in the spectral domain: the non-Galerkin characteristic (i.e., test functions different from the basis functions) has been chosen to ensure convergence of the spectral integrals defining the MoM matrix. The GNR is modeled through an appropriate

tensor surface-impedance boundary condition which takes into account the possible presence of static bias fields and also includes spatial-dispersion effects: this means that graphene is represented through a dyadic conductivity whose elements depend also on the spectral wavenumbers [8], [9]. It is worth noting that the effects of spatial dispersion on the electromagnetic properties of different graphene structures have recently been studied mainly in connection with infinite graphene-sheet structures [10]–[13] and it has been shown that they can dramatically change device performance. Although many studies have been devoted to SPP propagation in GNRs [4], [5], [14], to the best of our knowledge, none has fully addressed the issue of nonlocality (a preliminary investigation on nonlocal effects in GNRs has been presented in [15], but the authors used a low- q model that we will show below to be insufficient for correct modeling).

In the present study, we investigate how spatial dispersion affects the propagation properties along a GNR giving particular attention to the dispersion curves, current profiles, field distributions, and characteristic impedances of the fundamental SPP mode.

It is worth mentioning that, in the more general framework of using GNRs in graphene-based devices and circuits, two critical aspects are SPP excitation and graphene-metal contacts.

As concerns the excitation problem, which is a hot research topic, recent studies demonstrated excitation and detection of SPPs in graphene through near-field microscopy nanotips [16], [17]; however, the low excitation efficiency of such near-field sources has prompted research on alternative approaches based on free-space electromagnetic waves. In this case the main difficulty arises from the large momentum mismatch between plasmons and incoming waves, but different techniques have already been successfully developed in this connection, e.g., attenuated total reflection (ATR), scattering from a topological defect at the conductor surface, and Bragg scattering using diffraction gratings or a periodic corrugation of the surface of the conductor [18]–[20]. Although these techniques have been proposed in connection with infinite graphene sheets as well as arrays of GNRs, they may presumably be considered also for the excitation of a single GNR.

As concerns metal-graphene contacts, these constitute a potential limiting factor, especially in active devices, because of the possible occurrence of very large contact resistances, due to several physical and technological reasons, e.g., the low density of states in graphene compared with that of metals, the formation of dipoles and defects at the interface, etc. [21].

Manuscript received January 14, 2015; revised July 13, 2015; accepted September 02, 2015. Date of publication October 06, 2015; date of current version November 23, 2015. (Corresponding author: Giampiero Lovat.)

G. Lovat and R. Araneo are with DIAEE, University of Rome “Sapienza,” 00184 Rome, Italy (e-mail: giampiero.lovat@uniroma1.it).

P. Burghignoli is with DIET, University of Rome “Sapienza,” 00184 Rome, Italy.

G. W. Hanson is with the Department of Electrical Engineering, University of Wisconsin-Milwaukee, Milwaukee, WI 53211 USA.

Color versions of one or more of the figures in this paper are available online at <http://ieeexplore.ieee.org>.

Digital Object Identifier 10.1109/TTHZ.2015.2477600

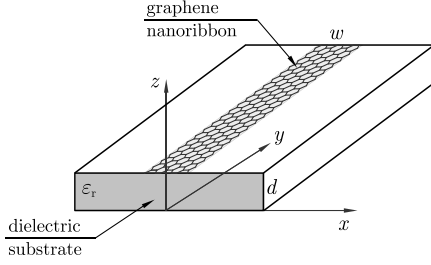


Fig. 1. GNR over a dielectric substrate. Parameters of the reference structure: $w = 200$ nm and $d = 400$ nm.

Both the considered topics, although important, are beyond the scope of the present investigation.

II. DESCRIPTION OF THE PROBLEM

The electromagnetic problem under analysis is sketched in Fig. 1. It consists of a graphene sheet of width w along the x -direction (i.e., a GNR) deposited on a laterally infinite dielectric substrate of thickness d along the z -direction and relative permittivity ϵ_r . All of the units are in the SI system and a time-harmonic variation $e^{j\omega t}$ is assumed and suppressed throughout. Propagation along the y -direction, i.e., modes with a spatial dependence $e^{-j\hat{q}_y y}$, is also assumed.

A. Graphene Conductivity

In general, a graphene sheet can be modeled as a conductive sheet with a dyadic surface conductivity [22]

$$\underline{\underline{\sigma}} = \begin{bmatrix} \sigma_{xx} & \sigma_{xy} \\ \sigma_{yx} & \sigma_{yy} \end{bmatrix}. \quad (1)$$

In the absence of magnetic bias and neglecting spatial dispersion, graphene can be simply characterized by a *scalar* local conductivity σ , which depends on external and internal parameters, e.g., radian frequency ω , temperature T , a phenomenological scattering rate $\Gamma = 1/\tau_s$ (where τ_s is the relaxation time depending on a variety of factors and determined experimentally), and the chemical potential μ_c (which can be controlled either through doping or through an applied bias electric field orthogonal to the graphene plate) [8]. Moreover, for the considered frequency range (i.e., below hundreds of THz), only the intraband contributions are considered, the interband terms being negligible [8]. In this case

$$\sigma(\omega) = \gamma \frac{\pi}{\alpha} \quad (2)$$

where

$$\gamma = -j \frac{q_e^2 k_B T}{\pi \hbar^2} \ln \left\{ 2 \left[1 + \cosh \left(\frac{\mu_c}{k_B T} \right) \right] \right\} \quad (3)$$

and $\alpha = \omega - j/\tau_s$, thus showing a Drude-like behavior. In (3) q_e is the electron charge, $v_F \simeq 10^6$ m/s is the Fermi velocity in graphene, while \hbar and k_B are the reduced Planck and the Boltzmann constants, respectively.

When a more refined model is considered which takes into account spatial dispersion, the graphene conductivity has a dyadic form, whose elements have been derived in [8] under a low- q

relaxation-time approximation (RTA) and, more recently, in [9] for arbitrary q values and with the Bhatnagar–Gross–Krook (BGK) model (which allows for including charge diffusion and deriving the correct quantum capacitance). For completeness, the expressions for the dyadic elements for different graphene conductivity models are reported in the Appendix.

B. Dispersion Analysis

Starting from the boundary condition $\tilde{\mathbf{E}}_t(q_x, q_y, z = h) = \underline{\underline{\sigma}}^{-1}(q_x, q_y) \cdot \tilde{\mathbf{J}}_S(q_x, q_y)$ on the GNR surface, the electric field integral equation (EFIE) can be expressed in the form

$$\begin{aligned} & \int_{-\infty}^{+\infty} \int_{-w/2}^{+w/2} \underline{\underline{\mathbf{G}}}^{\text{EJ}}(x-x', y-y', z=z'=h) \cdot \mathbf{J}_S(x', y') dx' dy' \\ &= \frac{1}{(2\pi)^2} \iint_{-\infty}^{+\infty} \underline{\underline{\rho}}(q_x, q_y) \cdot \tilde{\mathbf{J}}_S(q_x, q_y) e^{-j(q_x x + q_y y)} dq_x dq_y \end{aligned} \quad (4)$$

for $x \in (-w/2, w/2)$ and for any y , where $\underline{\underline{\mathbf{G}}}^{\text{EJ}}(\cdot)$ is the EJ-type dyadic Green function for planar layered media, $\tilde{\mathbf{J}}_S(q_x, q_y)$ is the Fourier transform of the modal surface current $\mathbf{J}_S(x, y)$, and $\underline{\underline{\rho}} = \underline{\underline{\sigma}}^{-1}$ is the dyadic resistivity. By introducing the spectral-domain Green's function $\tilde{\underline{\underline{\mathbf{G}}}}^{\text{EJ}}(q_x, q_y)$ and representing the surface current of the mode as

$$\mathbf{J}_S(x, y) = [J_x(x)\mathbf{u}_x + J_y(x)\mathbf{u}_y] e^{-j\hat{q}_y y} = \mathbf{J}_S(x) e^{-j\hat{q}_y y} \quad (5)$$

where $\hat{q}_y = \beta - j\alpha$ is the assumed propagation constant, after some manipulations, (4) can be rewritten as

$$\frac{1}{2\pi} \int_{-\infty}^{+\infty} \left[\tilde{\underline{\underline{\mathbf{G}}}}^{\text{EJ}}(q_x, \hat{q}_y) - \underline{\underline{\rho}}(q_x, \hat{q}_y) \right] \cdot \tilde{\mathbf{J}}_S(q_x) e^{-j\hat{q}_y x} dq_x = \mathbf{0} \quad (6)$$

for $x \in (-w/2, w/2)$, where $\tilde{\mathbf{J}}_S(q_x)$ is the Fourier transform of the modal surface current $\mathbf{J}_S(x)$.

Equation (6) is clearly a nonstandard eigenvalue equation: it has an infinite number of solutions, each of which identifies a propagation mode of the nanoribbon through its propagation constant $\hat{q}_{y,i}$ and its surface current distribution $\mathbf{J}_{S,i}$.

C. Numerical Solution

A standard MoM procedure can be used to solve the eigenvalue problem.

In particular, by expanding the x and y components of the modal current in M and N entire-domain (e.g., sinusoidal) basis functions $J_{x,m}$ and $J_{y,n}$, respectively, as

$$J_{Sx}(x) = \sum_{m=1}^M A_m J_{x,m}(x) \quad (7a)$$

$$J_{Sy}(x) = \sum_{n=0}^{N-1} B_n J_{y,n}(x) \quad (7b)$$

where A_m and B_n are unknown coefficients and

$$J_{x,m}(x) = \sin\left(\frac{2\pi m}{w} x\right), \quad m = 1, 2, \dots, M \quad (8a)$$

$$J_{y,n}(x) = \cos\left(\frac{2\pi n}{w} x\right), \quad n = 0, 1, \dots, N-1. \quad (8b)$$

It should be observed that the Fourier transforms of the basis functions in (8) are

$$\tilde{J}_{x,m}(q_x) = 4\pi j w \frac{m(-1)^m \sin\left(q_x \frac{w}{2}\right)}{(q_x w)^2 - (2m\pi)^2} \quad (9a)$$

$$\tilde{J}_{y,n}(q_x) = 2w^2 \frac{(-1)^n q_x \sin\left(q_x \frac{w}{2}\right)}{(q_x w)^2 - (2n\pi)^2}. \quad (9b)$$

By applying a *non-Galerkin* test procedure with test functions $T_{i,p/l}(x)$ ($i = x, y$), (6) can be recast in the following matrix form:

$$\begin{bmatrix} \tilde{Z}_{xx}^{pm}(\hat{q}_y) & \tilde{Z}_{xy}^{pn}(\hat{q}_y) \\ \tilde{Z}_{yx}^{lm}(\hat{q}_y) & \tilde{Z}_{yy}^{ln}(\hat{q}_y) \end{bmatrix} \begin{bmatrix} A_m \\ B_n \end{bmatrix} = \mathbf{0} \quad (10)$$

where $p = 1, \dots, M$, $l = 0, \dots, N - 1$, and

$$\begin{aligned} & \tilde{Z}_{rs}^{hq}(\hat{q}_y) \\ &= \int_{-\infty}^{+\infty} \tilde{T}_{r,h}(-q_x) \left[\tilde{G}_{rs}^{\text{EJ}}(q_x, \hat{q}_y) - \rho_{rs}(q_x, \hat{q}_y) \right] \tilde{J}_{s,q}(q_x) dq_x \end{aligned} \quad (11)$$

where $r, s = x, y$, $h = p, l$, $q = m, n$, and ρ_{rs} are the components of the dyadic resistivity $\underline{\rho}$. In particular, suitable test functions need to be chosen in order to ensure the convergence of the spectral integral in (11) [23]. This is not trivial, since it can be shown, based on the expressions derived in the Appendix, that in a full- q formulation we have

$$\rho_{xx} = \mathcal{O}(q_x^2), \quad \rho_{xy} = \rho_{yx} = \mathcal{O}(q_x), \quad \rho_{yy} = \mathcal{O}(q_x). \quad (12)$$

Hence, if the classical Galerkin test procedure were used, the integrand functions of the matrix elements $\tilde{Z}_{yy}^{ln}(\hat{q}_y)$ would show an asymptotic behavior as q_x^{-1} without alternating sign thus leading to non-convergent integrals.

A suitable choice of test functions is instead

$$T_{x,p}(x) = \sin\left(\frac{2\pi p}{w} x\right) \quad p = 1, 2, \dots, M \quad (13a)$$

$$T_{y,l}(x) = \cos\left[\frac{2\pi(l+1)}{w} x\right] + (-1)^l \quad l = 0, 1, \dots, N-1. \quad (13b)$$

The Fourier transform of (13a) is the same as in (9a), and it has an asymptotic behavior as $\mathcal{O}(q_x^{-2})$, while the Fourier transform of (13b) is

$$\tilde{J}_{y,l}(q_x) = 8\pi^2 \frac{(-1)^l l^2 \sin\left(q_x \frac{w}{2}\right)}{q_x^3 w^2 - 4q_x l^2 \pi^2} \quad (14)$$

with an asymptotic behavior as $\mathcal{O}(q_x^{-3})$ which ensures the convergence of all of the integrals (11).

The computation of the matrix elements in (11) involves the integration of functions which oscillate as $\sin^2(q_x w/2)$: the integration can then efficiently be performed through the double exponential formulas proposed in [24].

The eigenvalues \hat{q}_y have to be found searching for the *complex* zeroes of the determinant of the square $(M + N)$ matrix in (10), i.e.,

$$\det[\underline{\mathbf{Z}}(\hat{q}_y)] = 0 \quad (15)$$

and a dispersion analysis $\hat{q}_y(f)$ can easily be performed tracking the relevant complex pole as a function of the frequency f .

Although several methods are available for searching zeros on the complex plane [25], [26], the Müller's method is here employed since it is simple and robust. Since the number of iterations required to converge to the correct propagation constant (matrix eigenvalue) \hat{q}_y strictly depends on the initial guess, a suitable predictor has been developed based on an extrapolation procedure of the previous ten eigenvalues found at the previous frequencies. It results in a very efficient code that is able to track the eigenvalue at each frequency step with just three or four iterations.

D. Current, Field, and Characteristic Impedance Calculation

Once the propagation constant \hat{q}_y that makes null the determinant of the MoM matrix at a prescribed frequency is found, the eigenfunctions associated with the matrix $\underline{\mathbf{Z}}(\hat{q}_y)$ can easily be computed and the eigenfunction corresponding to the minimum eigenvalue (which is null within the machine accuracy) gives the expansion coefficients in (7); this way, both the longitudinal and transverse current components can easily be computed.

Once the modal current $\mathbf{J}_S(x, y)$ on the GNR surface is known, the modal field components can then be computed as

$$E_r(x, y, z) = \frac{e^{-j\hat{q}_y y}}{2\pi} \int_{-\infty}^{+\infty} \left[\tilde{G}_{rx}^{\text{EJ}}(q_x, \hat{q}_y; z) \tilde{J}_x(q_x) + \tilde{G}_{ry}^{\text{EJ}}(q_x, \hat{q}_y; z) \tilde{J}_y(q_x) \right] e^{-jq_x x} dq_x \quad (16a)$$

$$H_r(x, y, z) = \frac{e^{-j\hat{q}_y y}}{2\pi} \int_{-\infty}^{+\infty} \left[\tilde{G}_{rx}^{\text{HJ}}(q_x, \hat{q}_y; z) \tilde{J}_x(q_x) + \tilde{G}_{ry}^{\text{HJ}}(q_x, \hat{q}_y; z) \tilde{J}_y(q_x) \right] e^{-jq_x x} dq_x \quad (16b)$$

$$+ \tilde{G}_{ry}^{\text{HJ}}(q_x, \hat{q}_y; z) \tilde{J}_y(q_x) \right] e^{-jq_x x} dq_x \quad (16c)$$

where $r = \{x, y, z\}$ while $\tilde{\mathbf{G}}^{\text{EJ}}$ and $\tilde{\mathbf{G}}^{\text{HJ}}$ are the EJ- and HJ-type spectral-domain dyadic Green's functions, respectively [27]. It is worth noting that the computation of all of the involved integrals can be made more efficient by suitably exploiting the symmetries of the integrand functions.

The characteristic impedance is then calculated according to the current-power definition [28]

$$Z_c = 2 \frac{P}{|I|^2} = \frac{\int_{-\infty}^{\infty} \int_{-\infty}^{\infty} [\mathbf{E}(\mathbf{r}) \times \mathbf{H}^*(\mathbf{r})] \cdot \mathbf{u}_y dx dz}{\left| \int_{-w/2}^{w/2} J_y(x) dx \right|^2} \quad (17)$$

where the integral in the numerator of (17) is recursively computed over an increasing surface centered on the GNR and truncated when the prescribed accuracy is reached.

III. RESULTS

A. Graphene Conductivity and Basic Structure

Here, a comparison among the different graphene conductivity models is presented for different radian frequencies ω , assuming in all cases $\tau_s = 0.5$ ps, $\mu = 0$ eV, and $T = 300$ K. The conductivity dyadic will be represented in polar coordinates, showing results for the longitudinal and transverse conductivities σ_L and σ_T as functions of the radial wavenumber q normalized with respect to the free-space wavenumber k_0 [37].

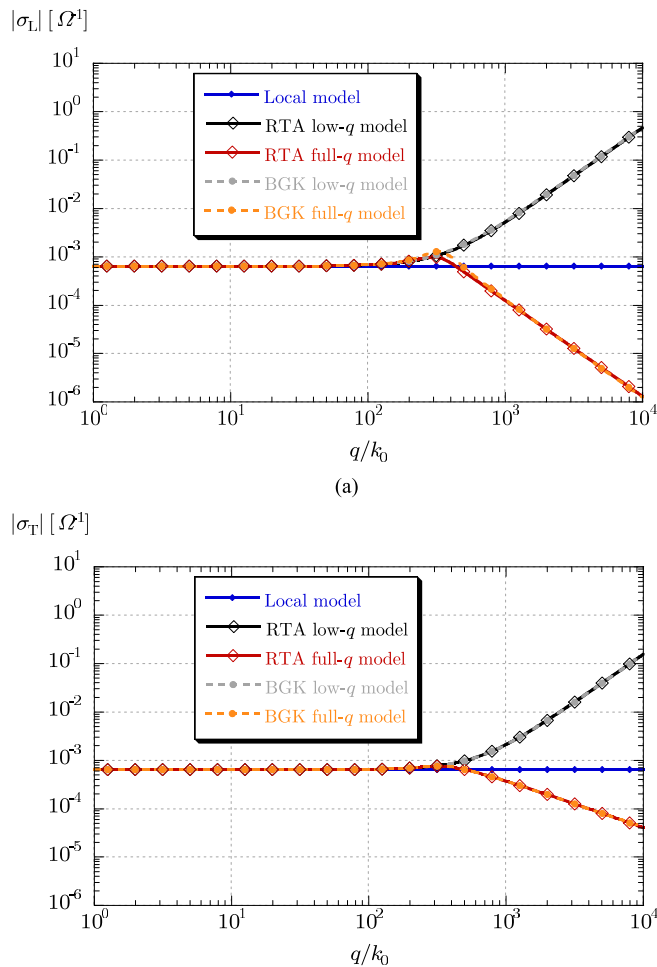


Fig. 2. Absolute values of (a) σ_L and (b) σ_T as functions of q/k_0 at $f = 1$ THz.

For clarity, we summarize the different models considered. For the RTA formulations there are two conductivity expressions: the full- q expression and the low- q approximation (cf. (33)–(34) and (28)–(29), respectively). For the BGK formulation, which is more accurate than the RTA, we also have two conductivity expressions: the full- q expression and the low- q approximation (cf. (30)–(31) and (26)–(27), respectively). We also show the scalar local model (2). Similar results have already been shown in [9], but we report them here for completeness and then focus on nonlocal GNR modal properties which have not been examined in detail.

In Fig. 2, the absolute values of σ_L and σ_T are shown at $\omega/(2\pi) = 1$ THz. For both components, the full- q RTA and BGK models are in excellent agreement, whereas the scalar local conductivity and both the low- q RTA and BGK models are accurate only in a low- q range, as expected; this range is however narrower for σ_L than for σ_T . In particular, it should be noted that the low- q formulations completely fail for large q , even more than the local model: this is to be expected since both the low- q elements have an asymptotic behavior as $\mathcal{O}(q^2)$, while the full- q longitudinal and transverse elements are $\mathcal{O}(q^{-2})$ and $\mathcal{O}(q^{-1})$, respectively (the local formulation is instead independent of q , i.e., $\mathcal{O}(q^0)$).

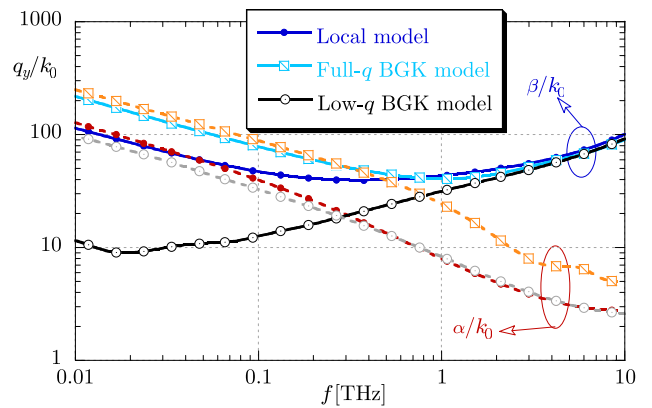


Fig. 3. Normalized phase (β/k_0) and attenuation (α/k_0) constants as functions of frequency f for a structure as in Fig. 1 with $\epsilon_r = 1$. Different conductivity models are considered: a local model, a low- q BGK model, and a full- q BGK model.

In order to show the effects of spatial dispersion on the electromagnetic properties of GNRs, we consider a GNR structure with $w = 200$ nm (more than two orders of magnitude larger than the graphene lattice constant a , so that electronic edge-effects can be ignored) and $d = 400$ nm, with different permittivity values for the substrate. All of the results have been obtained with six basis functions for each current component (i.e., $M = N = 6$) which provide converged results.

B. SPP Propagation Characteristics

In Fig. 3, the dispersion properties of the fundamental SPP mode supported by a free-standing GNR (i.e., $\epsilon_r = 1$) are reported in a logarithmic scale. In particular, the normalized phase ($\beta/k_0 = \Re\{q_y/k_0\}$) and attenuation ($\alpha/k_0 = -\Im\{q_y/k_0\}$) constants are plotted as functions of frequency by adopting three different conductivity models for graphene, i.e., a local formulation, a low- q BGK formulation, and a full- q BGK formulation. The latter fully takes into account the nonlocal effects which are seen to be particularly pronounced in the lowest (microwave) frequency range. On the other hand, as expected, the low- q formulation leads to erroneous results especially in the lowest frequency range (this happens both in the RTA and BGK formulations).

In Fig. 4(a) and (b), the normalized phase β/k_0 and attenuation α/k_0 constants are reported as functions of frequency for a free-standing GNR with different ribbon widths: from Fig. 4, it can thus be seen that nonlocal effects are stronger for ribbons with narrower widths and negligible for ribbons with widths larger than $1 \mu\text{m}$.

In Fig. 5(a) and (b), the dispersion properties are reported for a GNR with two different permittivities of the substrate, i.e., a moderate permittivity $\epsilon_r = 3.9$ [Fig. 5(a)] and a high permittivity $\epsilon_r = 10.2$ [Fig. 5(b)]. In these cases the low- q results have not been reported since it can be shown that such a low- q formulation dramatically fails. On the other hand, it can easily be seen that increasing the dielectric permittivity strongly enhances the spatial-dispersion effects, as shown in [11] for modes supported by an infinite graphene sheet. In particular, it can be seen that in the high-permittivity case ignoring spatial dispersion leads

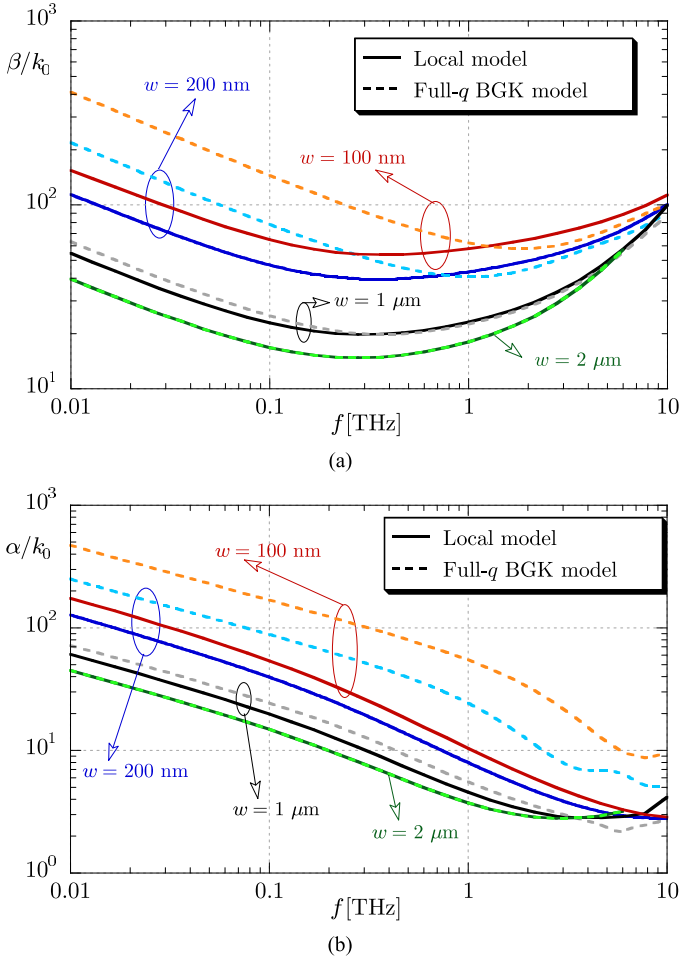


Fig. 4. Normalized propagation constants as functions of frequency f for a structure as in Fig. 1 with $\varepsilon_r = 1$ for different ribbon widths. Two different conductivity models are considered, i.e., a local model and a full- q BGK model for the calculation of (a) the normalized phase constant β/k_0 and (b) the normalized attenuation constant α/k_0 .

to relative errors in the calculation of the phase and attenuation constants which are both larger than 50% at 10 THz: at low frequencies such errors are still larger. In the considered frequency range, including spatial dispersion increases the attenuation constant of the plasmon mode, except for the high-permittivity case in the higher part of the frequency spectrum: in such a case, e.g., at $f = 10$ THz, spatial dispersion leads to an attenuation constant much lower than that of the local formulation. Instead, as concerns the phase constant, spatial dispersion makes the plasmon mode much slower at lower frequencies and much faster at higher frequencies.

C. Modal Currents and Field Distributions

In Fig. 6, the amplitude of the longitudinal y -component J_y of the modal current along the nanoribbon (normalized to its maximum value) is reported at the operating frequency $f = 1$ THz for a structure as in Fig. 3. The transverse x -component J_x is not reported since its value is more than three-orders of magnitude smaller than the longitudinal component J_y . It can be seen that ignoring spatial dispersion or using a spatially-dispersive model valid for low wave numbers leads to completely erroneous current profiles. In particular, the almost constant behavior typical

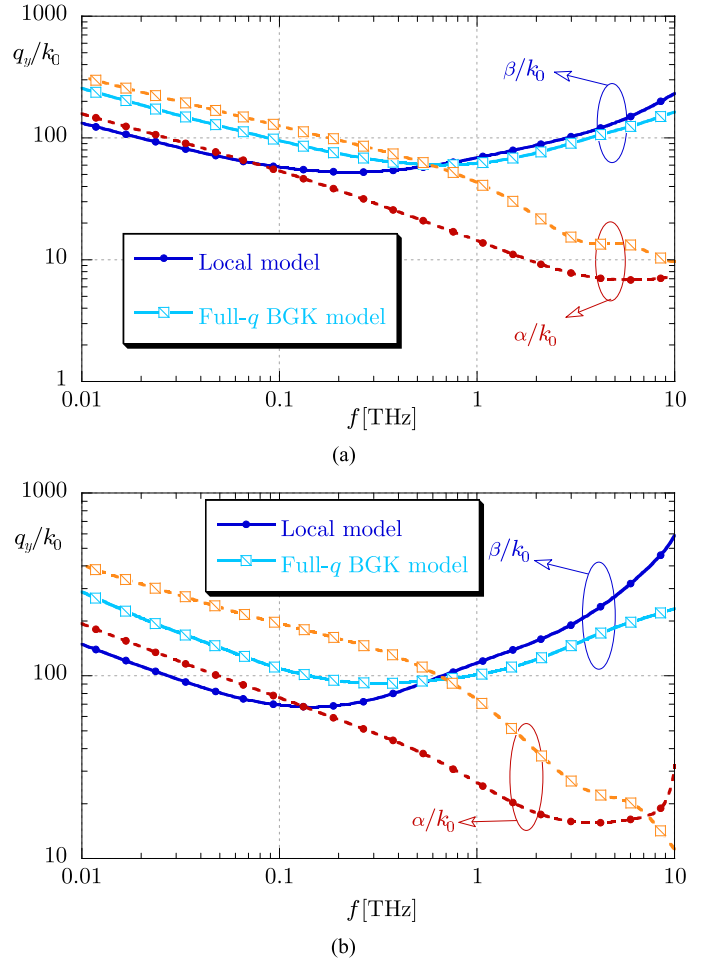


Fig. 5. Normalized phase (β/k_0) and attenuation (α/k_0) constants as functions of frequency f for a structure as in Fig. 1 with (a) $\varepsilon_r = 3.9$ and (b) $\varepsilon_r = 10.2$. Two different conductivity models are considered, i.e., a local model and a full- q BGK model.

of the fundamental mode in microwave microstrip line is obtained using a purely local model, whereas the correct spatially dispersive full- q conductivity formulation determines a variable current profile across the ribbon with a minimum at the edges and a maximum near the center of the graphene nanoribbon. Such a behavior is exactly the opposite of what is found adopting a low- q model which predicts a current profile far from both the purely local model and the correct spatially dispersive model. Again, using a low- q model in such problems dramatically affects the correctness of the results.

It is worth noting that the behavior shown in Fig. 6 is qualitatively the same across the considered frequency spectrum (from 10 GHz to 10 THz) and for structures with different substrate permittivities.

The normalized electric and magnetic field distributions are reported in Fig. 7(a) and (b), respectively, for a structure as in Fig. 6 (i.e., $\varepsilon_r = 1$ and $f = 1$ THz). They show a classical 2-D monopole-like behavior and have been obtained using the full- q conductivity formulation. A local model would lead to the same qualitative field behavior: to observe the quantitative differences, in Fig. 8(a) the amplitude of the normalized electric fields are reported as functions of z for $x = 0$ at $f = 1$ THz

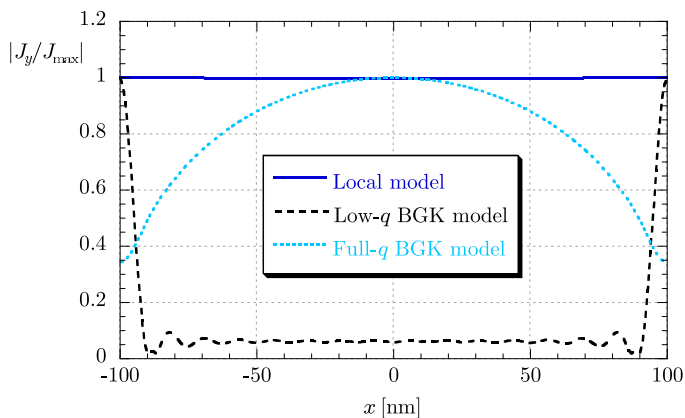


Fig. 6. Normalized y -component of the modal current J_y across the nanoribbon for a structure as in Fig. 1 with $\epsilon_r = 1$ and $f = 1$ THz. Different conductivity models are considered: a local model, a low- q BGK model, and a full- q BGK model.

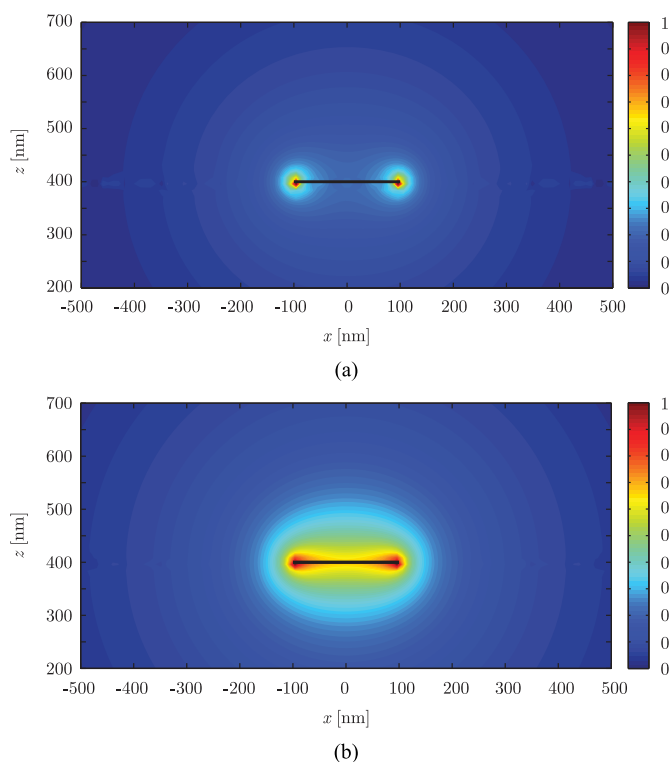
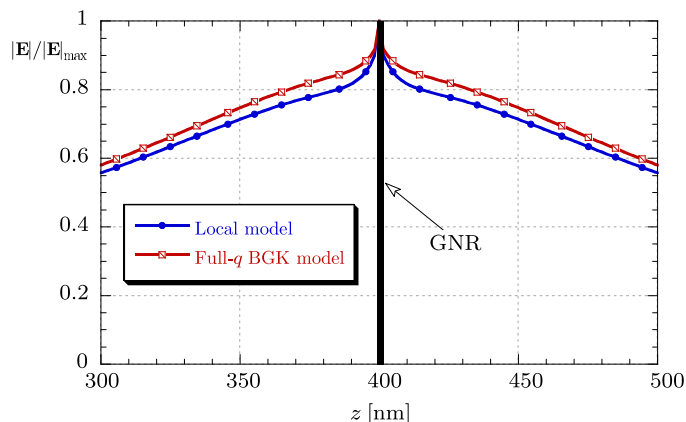
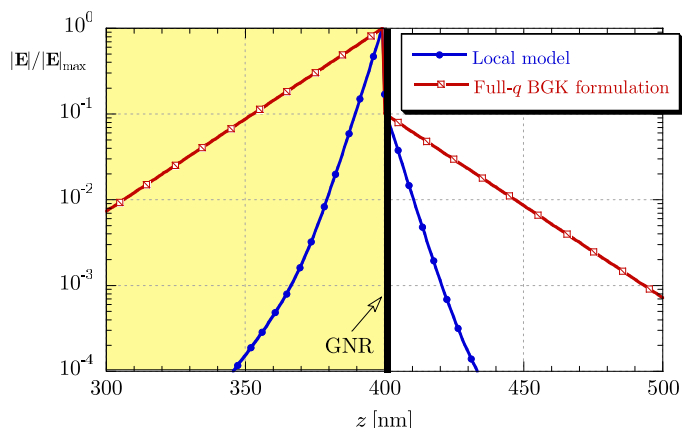


Fig. 7. Normalized (a) electric and (b) magnetic field distribution of the plasmon mode for a structure as in Fig. 6 using a full- q BGK model.

for a free-standing GNR. In order to point out the spatial-dispersion effects in the modal field distributions of GNRs the same of Fig. 8(a) is reported in Fig. 8(b) for a structure with $\epsilon_r = 10.2$ and at $f = 10$ THz. It can be seen that, while in the former case the plasmon mode is poorly confined and spatial-dispersion effects are negligible, in the latter the electric field is well concentrated near the ribbon, although the inclusion of spatial dispersion greatly reduces the amount of field confinement. This also occurs for, e.g., localized surface plasmons, where spatial dispersion reduces the field concentration in the gap between two plasmonic dimers [29].



(a)



(b)

Fig. 8. Amplitude of the normalized electric field as a function of z for a structure as in Fig. 1. Parameters: (a) $\epsilon_r = 1$ and $f = 1$ THz and (b) $\epsilon_r = 10.2$ and $f = 10$ THz.

D. Characteristic Impedance

The real and imaginary parts of the characteristic impedance are reported as functions of frequency in Fig. 9(a) for a free-standing GNR as in Figs. 3 and in Figs. 9(b) for a high-dielectric GNR as in Fig. 5(b). As it can be seen, at low frequencies, both the real and imaginary parts are of the order of $k\Omega$, and there is a significant discrepancy between the local model and the full- q BGK formulation: such a discrepancy disappears beyond 1 THz for the real part and beyond 2 THz the imaginary part become one order of magnitude smaller than the real part. Interestingly, the spatial-dispersion effects on the characteristic impedance of the GNR are weaker in the high-permittivity case.

E. Electrical Conductivity Tuning

As is well known, one of the most attractive characteristic of graphene is the possibility of externally controlling its electrical conductivity by modifying the chemical potential μ_c : this can be obtained either by applying an electrostatic bias or by doping [8]. In a more general framework, such an external tuning could be used to dynamically control the reflection, absorption, or polarization of the electromagnetic waves impinging against a graphene shield [30], to control the radiation characteristics of leaky-wave antennas [31], or to make graphene layers working as tunable cloaks [32]. Moreover, in recent works it has been

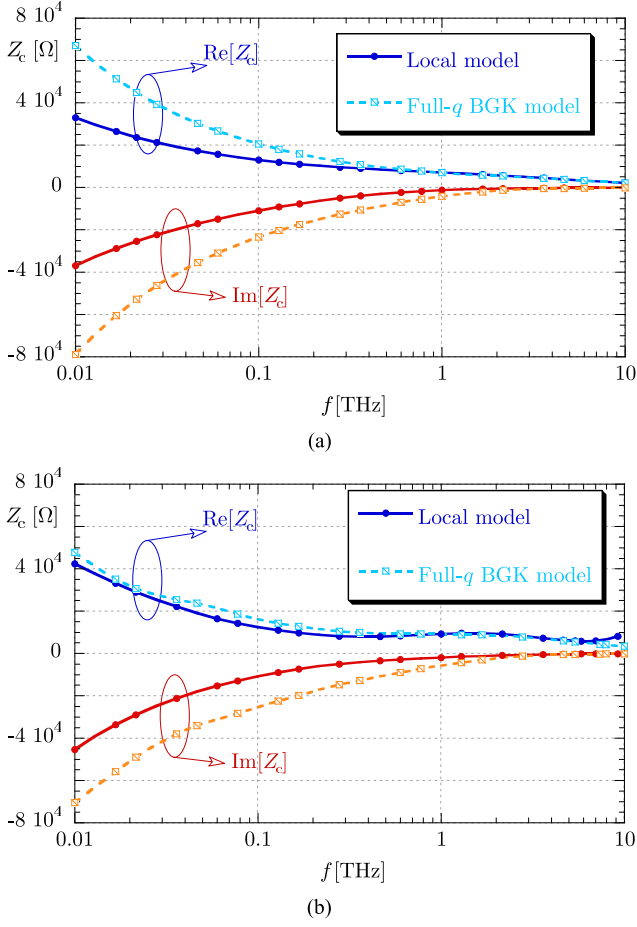


Fig. 9. Real and imaginary parts of the characteristic impedance of (a) a free-standing and (b) a high-dielectric GNR as in Fig. 1.

shown that graphene can effectively act as a platform for infrared metamaterials and transformation optical devices [33], [34]. For plasmon propagation in GNRs, the conductivity tuning allows for varying the chemical potential across the strip (thus generating a nonhomogeneous conductivity), or for creating different channels for propagation over a uniform sheet [35]. The analysis of inhomogeneous GNRs is out of the scope of the present investigation and it requires different numerical tools [36]; rather, it is here interesting to investigate the effects of a uniform variation of the chemical potential μ_c on the propagation features of the dominant plasmon mode in GNRs, i.e., we consider a GNR with a homogeneous conductivity whose value can be tuned at a fixed frequency by externally varying the chemical potential μ_c .

In Fig. 10 the normalized phase and attenuation constants are reported as functions of the chemical potential μ_c for a structure as in Fig. 1 with $\epsilon_r = 1$ at the operating frequency $f = 1$ THz. As for the dispersion analysis, two different conductivity models are considered, i.e., a local model and a full- q BGK formulation for the graphene conductivity. It can be seen that the influence of the chemical potential on the propagation properties of GNRs is the same for the local and the spatially-dispersive model: in fact, a variation of μ_c only affects the term γ in (3). By increasing μ_c , the real part of the conductivity (which is responsible of losses) decreases and, accordingly, the attenuation constant of the propagating

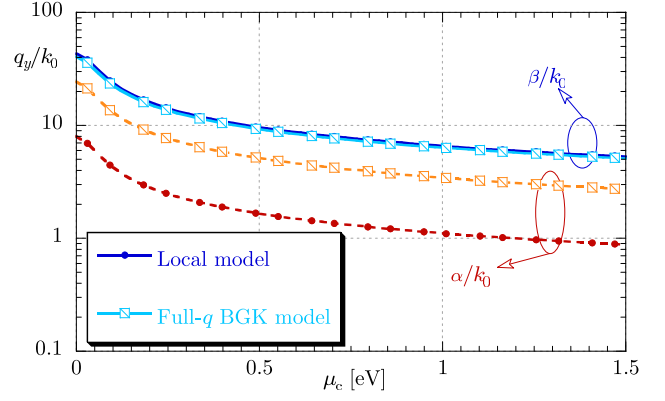


Fig. 10. Normalized phase (β/k_0) and attenuation (α/k_0) constants as functions of the chemical potential μ_c for a structure as in Fig. 1 with $\epsilon_r = 1$ at the operating frequency $f = 1$ THz.

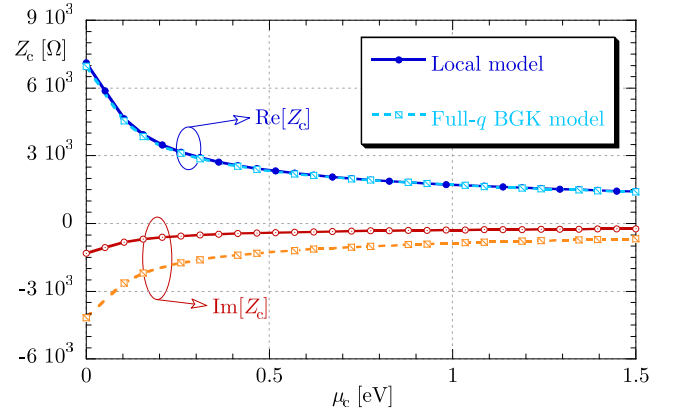


Fig. 11. Real and imaginary parts of the characteristic impedance of a GNR as in Fig. 1 with $\epsilon_r = 1$ at the operating frequency $f = 1$ THz as functions of the chemical potential μ_c .

plasmon mode also decreases: such a decreasing is more pronounced for small values of μ_c . Although reported in Fig. 10 for a particular configuration of GNRs, such a behavior is general, as verified by numerous simulations.

In Fig. 11, the real and imaginary parts of the characteristic impedance of the same structure as in Fig. 10 are reported as function of the chemical potential μ_c . These results have been obtained using a local model and a full- q BGK formulation for the graphene conductivity. As can be seen, the variation of the chemical potential can tune the values of the characteristic impedance by reducing it by about 80%.

IV. DISCUSSION AND CONCLUSION

Nonlocal effects that severely affect the propagation properties of the fundamental plasmon mode in graphene nanoribbons have been carefully investigated by means of a Method-of-Moments approach in the spectral domain which fully takes into account the spatially dispersive nature of the intraband graphene conductivity. Results have been presented for the propagation constant, the current profile, the field patterns, and the characteristic impedance of the dominant plasmon mode showing that spatial dispersion have to be taken into account through a model valid for arbitrarily large q value if dramatic errors are to be avoided.

In particular, it has been shown that the strongest nonlocal effects occur for GNRs with small widths and supported by a dielectric with high permittivity: usually the nonlocality largely attenuates the longitudinal propagation of the plasmon mode and makes it slower at low frequencies and faster at high frequencies. The transverse profile of the longitudinal component of the current is strongly modified showing a maximum at the center of the ribbon, while the modal field is less tightly confined to the ribbon. The characteristic impedance is less affected by spatial dispersion, at least for high frequencies, whereas in the low frequency (microwave) regime can be largely increased both in its resistive and capacitive part. Bias voltages or chemical doping can be effectively used to tune the modal properties of the propagating SPP and, in particular, the former can be used to locally modify the transverse conductivity profile to create a tunable inhomogeneous conductivity (this is left for future works).

As concerns the effects that nonlocality may have on graphene-based devices, the large variety of structures proposed in recent years, e.g., phase-shifters, filters, absorbers, prevents one from drawing sharp conclusions. However, in the light of the results obtained in the present investigation, our feeling is that nonlocality does not necessarily spoil the expected performance of GNR-based components, but, rather, it is a key parameter that must be taken into account in proper device modeling and design.

APPENDIX

For completeness, we report in this Appendix the expressions of the dyadic elements for different graphene conductivity models derived in [9]. In particular, we show in a low- q RTA model

$$\begin{aligned}\sigma_{xx}^{\text{RTA}} &= \gamma \frac{\pi}{\alpha} \left(1 + \frac{3v_{\text{F}}^2}{4\alpha^2} q_x^2 + \frac{v_{\text{F}}^2}{4\alpha^2} q_y^2 \right) \\ \sigma_{xy}^{\text{RTA}} &= \gamma \frac{\pi}{\alpha} \left(\frac{v_{\text{F}}^2}{2\alpha^2} \right) q_x q_y \\ \sigma_{yx}^{\text{RTA}} &= \gamma \frac{\pi}{\alpha} \left(\frac{v_{\text{F}}^2}{2\alpha^2} \right) q_x q_y \\ \sigma_{yy}^{\text{RTA}} &= \gamma \frac{\pi}{\alpha} \left(1 + \frac{v_{\text{F}}^2}{4\alpha^2} q_x^2 + \frac{3v_{\text{F}}^2}{4\alpha^2} q_y^2 \right)\end{aligned}\quad (18)$$

whereas in a low- q BGK model we have

$$\begin{aligned}\sigma_{xx}^{\text{BGK}} &\simeq \gamma \frac{\pi}{\alpha} \left[1 + \frac{v_{\text{F}}^2}{4\alpha^2} \left(3 + i \frac{2}{\omega\tau} \right) q_x^2 + \frac{v_{\text{F}}^2}{4\alpha^2} q_y^2 \right] \\ \sigma_{xy}^{\text{BGK}} &\simeq \gamma \frac{\pi}{\alpha} \left(\frac{v_{\text{F}}^2}{2\alpha^2} \right) \left(1 + i \frac{1}{\omega\tau} \right) q_x q_y \\ \sigma_{yx}^{\text{BGK}} &\simeq \gamma \frac{\pi}{\alpha} \left(\frac{v_{\text{F}}^2}{2\alpha^2} \right) \left(1 + i \frac{1}{\omega\tau} \right) q_x q_y \\ \sigma_{yy}^{\text{BGK}} &\simeq \gamma \frac{\pi}{\alpha} \left[1 + \frac{v_{\text{F}}^2}{4\alpha^2} q_x^2 + \frac{v_{\text{F}}^2}{4\alpha^2} \left(3 + i \frac{2}{\omega\tau} \right) q_y^2 \right].\end{aligned}\quad (19)$$

In an RTA model, the dyadic conductivity elements whose expressions are instead valid for arbitrary values of q are

$$\underline{\sigma}^{\text{RTA}} = \gamma \underline{\mathbf{I}}_{\phi} \quad (20)$$

where

$$\begin{aligned}I_{\phi_{xx}}(q_x, q_y) &= 2\pi \frac{v_{\text{F}}^2 q_y^2 q^2 R - \alpha v_{\text{F}} q_x p^2 - \alpha^2 p^2 (1-R)}{v_{\text{F}}^2 (\alpha + v_{\text{F}} q_x) q^4} \\ I_{\phi_{xy}}(q_x, q_y) &= I_{\phi_{yx}}(q_x, q_y) \\ &= -2\pi q_x q_y \frac{v_{\text{F}}^2 q^2 R + 2\alpha v_{\text{F}} q_x + 2\alpha^2 (1-R)}{v_{\text{F}}^2 (\alpha + v_{\text{F}} q_x) q^4} \\ I_{\phi_{yy}}(q_x, q_y) &= 2\pi \frac{v_{\text{F}}^2 q_x^2 q^2 R + \alpha v_{\text{F}} q_x p^2 + \alpha^2 p^2 (1-R)}{v_{\text{F}}^2 (\alpha + v_{\text{F}} q_x) q^4}\end{aligned}\quad (21)$$

with $q^2 = q_x^2 + q_y^2$, $p^2 = q_x^2 - q_y^2$, and

$$R(q_x, q_y) = \frac{\alpha + v_{\text{F}} q_x}{\sqrt{\alpha^2 - v_{\text{F}}^2 q^2}}. \quad (22)$$

In a BGK full- q model, we have

$$\begin{aligned}\sigma_{xx}^{\text{BGK}} &= \gamma \frac{I_{\phi_{xx}} + \gamma_{\text{D}} \Delta q_y (I_{\phi_{xx}} q_y - I_{\phi_{yx}} q_x)}{D_{\sigma}} \\ \sigma_{xy}^{\text{BGK}} &= \gamma \frac{I_{\phi_{xy}} + \gamma_{\text{D}} \Delta q_y (I_{\phi_{xy}} q_y - I_{\phi_{yy}} q_x)}{D_{\sigma}} \\ \sigma_{yx}^{\text{BGK}} &= \gamma \frac{I_{\phi_{yx}} + \gamma_{\text{D}} \Delta q_x (I_{\phi_{yx}} q_x - I_{\phi_{xx}} q_y)}{D_{\sigma}} \\ \sigma_{yy}^{\text{BGK}} &= \gamma \frac{I_{\phi_{yy}} + \gamma_{\text{D}} \Delta q_x (I_{\phi_{yy}} q_x - I_{\phi_{xy}} q_y)}{D_{\sigma}}\end{aligned}\quad (23)$$

where

$$\gamma_{\text{D}} = j \frac{v_{\text{F}}}{2\pi\omega\tau} \quad (24)$$

and $D_{\sigma} = 1 + \gamma_{\text{D}} \Delta q^2$ with

$$\Delta(q_x, q_y) = -\frac{2\pi}{v_{\text{F}} q^2} \left(1 - \frac{\alpha}{\sqrt{\alpha^2 - v_{\text{F}}^2 q^2}} \right). \quad (25)$$

Simpler expressions can be obtained in a polar coordinate system through the conventional longitudinal σ_{L} and transverse σ_{T} representation [37]. In particular, in a low- q approximation

$$\sigma_{\text{L}}^{\text{BGK}} = \gamma \frac{\pi}{\alpha} \left[1 + \left(\frac{3}{4} + i \frac{1}{2\omega\tau} \right) \frac{v_{\text{F}}^2}{\alpha^2} q^2 \right] \quad (26)$$

$$\sigma_{\text{T}}^{\text{BGK}} = \gamma \frac{\pi}{\alpha} \left(1 + \frac{v_{\text{F}}^2}{4\alpha^2} q^2 \right) \quad (27)$$

while

$$\sigma_{\text{L}}^{\text{RTA}} = \gamma \frac{\pi}{\alpha} \left[1 + \frac{3v_{\text{F}}^2}{4\alpha^2} q^2 \right] \quad (28)$$

and

$$\sigma_{\text{T}}^{\text{RTA}} = \sigma_{\text{T}}^{\text{BGK}} \quad (29)$$

whereas the relevant full- q expressions are

$$\sigma_{\text{L}}^{\text{BGK}} = \frac{v_{\text{F}}}{2\pi\gamma_{\text{D}} (1-\chi) + v_{\text{F}}\chi} \sigma_{\text{T}}^{\text{BGK}} \quad (30)$$

$$\sigma_{\text{T}}^{\text{BGK}} = \gamma \frac{2\pi\alpha}{v_{\text{F}}^2 q^2} (1-\chi) \quad (31)$$

with

$$\chi = \sqrt{1 - \frac{v_{\text{F}}^2 q^2}{\alpha^2}} \quad (32)$$

for the BGK model and

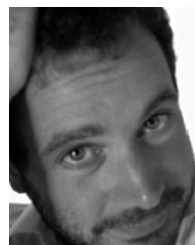
$$\sigma_T^{\text{RTA}} = \frac{1}{\chi} \sigma_L^{\text{RTA}} \quad (33)$$

$$\sigma_L^{\text{RTA}} = \sigma_L^{\text{BGK}} \quad (34)$$

for the RTA model. It should be noted that both σ_L and σ_T always depend only on q . This indicates that, in the absence of magnetic bias, graphene is modeled as an isotropic medium, the dyadic nature of its conductivity being uniquely due to the occurrence of spatial dispersion.

REFERENCES

- [1] C. Xu, H. Li, and K. Banerjee, "Modeling, analysis, and design of graphene nano-ribbon interconnects," *IEEE Trans. Electron Devices*, vol. 56, no. 8, pp. 1567–1578, Aug. 2009.
- [2] Y.-M. Lin, A. Valdes-Garcia, S.-J. Han, D. B. Farmer, I. Meric, Y. Sun, Y. Wu, C. Dimitrakopoulos, A. Grill, P. Avouris, and K. A. Jenkins, "Wafer-scale graphene integrated circuits," *Science*, vol. 332, no. 10, pp. 1294–1297, Mar. 2011.
- [3] J.-P. Cui, W.-S. Zhao, W.-Y. Yin, and J. Hu, "Signal transmission analysis of multilayer graphene nano-ribbon (MLG NR) interconnects," *IEEE Trans. Electromagn. Compat.*, vol. 54, no. 1, pp. 126–132, Feb. 2012.
- [4] A. Y. Nikitin, F. Guinea, F. J. García-Vidal, and L. Martín-Moreno, "Edge and waveguide TERAHERTZ surface plasmon modes in graphene microribbons," *Phys. Rev. B*, vol. 84, Oct. 2011, Art. ID 161407.
- [5] J. Christensen, A. Manjavacas, S. Thongrattanasiri, F. H. L. Koppens, and F. J. García de Abajo, "Graphene plasmon waveguiding and hybridization in individual and paired nanoribbons," *ACS Nano*, vol. 6, no. 1, pp. 431–440, 2012.
- [6] F. H. L. Koppens, D. E. Chang, and F. J. García de Abajo, "Graphene plasmonics: A platform for strong light-matter interactions," *Nano Lett.*, vol. 11, no. 8, pp. 3370–3377, 2011.
- [7] M. Jablan, M. Soljagic, and H. Buljan, "Plasmons in graphene: Fundamental properties and potential applications," *Proc. IEEE*, vol. 101, no. 7, pp. 1689–1704, Sep. 2013.
- [8] G. W. Hanson, "Dyadic Green's functions for an anisotropic non-local model of biased graphene," *IEEE Trans. Antennas Propag.*, vol. 56, no. 3, pp. 747–757, Mar. 2008.
- [9] G. Lovat, G. W. Hanson, R. Araneo, and P. Burghignoli, "Semiclassical spatially dispersive intraband conductivity tensor and quantum capacitance of graphene," *Phys. Rev. B*, vol. 87, no. 11, Mar. 2013, Art. ID 115429.
- [10] G. Lovat, P. Burghignoli, and R. Araneo, "Low-frequency dominant-mode propagation in spatially-dispersive graphene nano-waveguides," *IEEE Trans. Electromagn. Compat.*, vol. 55, no. 1, pp. 101–109, Feb. 2013.
- [11] J. Gomez-Diaz, J. Mosig, and J. Perruisseau-Carrier, "Effect of spatial dispersion on surface waves propagating along graphene sheets," *IEEE Trans. Antennas Propag.*, vol. 61, no. 7, pp. 3589–3596, Jul. 2013.
- [12] D. Correas-Serrano, J. Gomez-Diaz, J. Perruisseau-Carrier, and A. Alvarez-Melcon, "Spatially dispersive graphene single and parallel plate waveguides: Analysis and circuit model," *IEEE Trans. Microw. Theory Techn.*, vol. 61, no. 12, pp. 4333–4344, Dec. 2013.
- [13] D. Correas-Serrano, J. Gomez-Diaz, and A. Alvarez-Melcon, "On the influence of spatial dispersion on the performance of graphene-based plasmonic devices," *IEEE Antennas Wireless Propag. Lett.*, vol. 13, pp. 345–348, 2014.
- [14] X. Zhu, W. Yan, N. A. Mortensen, and S. Xiao, "Bends and splitters in graphene nanoribbon waveguides," *Opt. Exp.*, vol. 21, no. 3, pp. 3486–3491, Feb. 2013.
- [15] W. Wang and J. M. Kinaret, "Plasmons in graphene nanoribbons: Interband transitions and nonlocal effects," *Phys. Rev. B*, vol. 87, May 2013, Art. ID 195424.
- [16] J. Chen *et al.*, "Optical nano-imaging of gate tunable graphene plasmons," *Nature*, vol. 487, no. 7405, pp. 77–81, 2012.
- [17] Z. Fei *et al.*, "Gate-tuning of graphene plasmons revealed by infrared nano-imaging," *Nature*, vol. 487, no. 7405, pp. 82–85, 2012.
- [18] W. Gao, J. Shu, C. Qiu, and Q. Xu, "Excitation of plasmonic waves in graphene by guided-mode resonances," *ACS Nano*, vol. 6, no. 9, pp. 7806–7813, 2012.
- [19] W. Gao, G. Shi, Z. Jin, J. Shu, Q. Zhang, R. Vajtai, P. M. Ajayan, J. Kono, and Q. Xu, "Excitation and active control of propagating surface plasmon polaritons in graphene," *Nano Lett.*, vol. 13, pp. 3698–3702, 2013.
- [20] Y. Bludov, A. Ferreira, N. M. R. Peres, and M. I. Vasilevskiy, "A primer on surface plasmon-polaritons in graphene," *Int. J. Mod. Phys. B*, vol. 27, no. 10, 2013, Art. ID 1341001.
- [21] W. Liu, J. Wei, X. Sun, and H. Yu, "A study on graphene—metal contact," *Crystals*, vol. 3, no. 1, pp. 257–274, 2013.
- [22] L. A. Falkovsky, "Optical properties of graphene and IV – VI semiconductors," *Physics-Uspekhi*, vol. 51, no. 9, p. 887, 2008.
- [23] M. Havrilla and D. Nyquist, "Full-wave analysis of an imperfectly-conducting stripline," *J. Electromagn. Waves Applicat.*, vol. 16, no. 6, pp. 739–755, 2002.
- [24] T. Ooura and M. Mori, "A robust double exponential formula for Fourier-type integrals," *J. Comput. Appl. Math.*, vol. 112, pp. 229–241, 1999.
- [25] C. Gillan, A. Schuchinsky, and L. Spence, "Computing zeros of analytic functions in the complex plane without using derivatives," *Comput. Phys. Commun.*, vol. 175, no. 4, pp. 304–313, Aug. 2006.
- [26] R. Rodriguez-Berral, F. Mesa, and F. Medina, "Systematic and efficient root finder for computing the modal spectrum of planar layered waveguides," *Int. J. RF Microw. Comput. Eng.*, vol. 14, no. 1, pp. 73–83, Jan. 2004.
- [27] K. A. Michalski and J. R. Mosig, "Multilayered media Green's functions in integral equation formulations," *IEEE Trans. Antennas Propag.*, vol. 45, no. 3, pp. 508–519, Mar. 1997.
- [28] J. Brews, "Characteristic impedance of microstrip lines," *IEEE Trans. Microw. Theory Techn.*, vol. MTT-35, no. 1, pp. 30–34, Jan. 1987.
- [29] F. J. García de Abajo, "Nonlocal effects in the plasmons of strongly interacting nanoparticles, dimers, and waveguides," *J. Phys. Chemistry C*, vol. 112, no. 46, pp. 17983–17987, 2008.
- [30] A. Fallahi and J. Perruisseau-Carrier, "Design of tunable bi-periodic graphene metasurfaces," *Phys. Rev. B*, vol. 86, Nov. 2012, Art. ID 195408.
- [31] M. Esquius-Morote, J. Gomez-Diaz, and J. Perruisseau-Carrier, "Sinusoidally modulated graphene leaky-wave antenna for electronic beam-scanning at THz," *IEEE Trans. THz Sci. Technol.*, vol. 4, no. 1, pp. 116–122, Jan. 2014.
- [32] P.-Y. Chen and A. Alù, "Atomically thin surface cloak using graphene monolayers," *ACS Nano*, vol. 5, no. 7, pp. 5855–5863, 2011.
- [33] A. Vakil and N. Engheta, "Transformation optics using graphene," *Science*, vol. 332, no. 6035, pp. 1291–1294, 2011.
- [34] S. Maci, G. Minatti, M. Casaletti, and M. Bosiljevac, "Metasurfing: Addressing waves on impenetrable metasurfaces," *IEEE Antennas Wireless Propag. Lett.*, vol. 10, pp. 1499–1502, 2011.
- [35] E. Forati and G. W. Hanson, "Soft-boundary graphene nanoribbon formed by a graphene sheet above a perturbed ground plane: Conductivity profile and SPP modal current distribution," *J. Opt.*, vol. 16, no. 8, p. 089501, 2014.
- [36] P. Burghignoli, R. Araneo, G. Lovat, and G. Hanson, "Space-domain method of moments for graphene nanoribbons," in *Proc. 8th Eur. Conf. Antennas and Propagat.*, Apr. 2014, pp. 666–669.
- [37] M. Dressel and G. Grüner, *Electrodynamics of Solids*. Cambridge, U.K.: Cambridge Univ., 2002.



Giampiero Lovat (S'02–M'06) received the Ph.D. degree in applied electromagnetics from the University of Rome "Sapienza", Rome, Italy, in 2005.

He is currently an Assistant Professor with the Astronautical, Electrical, and Energetic Engineering Department, University of Rome "Sapienza", Rome, Italy. He is a coauthor of "Fast Breaking Papers, October 2007" in EE and CS, about metamaterials. He coauthored the book *Electromagnetic Shielding* (IEEE–Wiley, 2008). His present research interests include leaky waves, periodic structures, electromagnetic shielding, and nanoelectromagnetics.

Dr. Lovat was the recipient of the Young Scientist Award from the 2005 URSI General Assembly, New Delhi, India, and in 2011, he was the recipient of the Best Paper Symposium Award at the 2011 IEEE EMC-S International Symposium on Electromagnetic Compatibility.



Rodolfo Araneo (M'03–SM'10) received the Ph.D. degree in electrical engineering from the University of Rome “Sapienza”, Rome, in 2002.

He was a Visiting Student with the National Institute of Standards and Technology (NIST) Boulder, CO, USA, where he worked on TEM cells and shielding, and a Visiting Researcher of the Department of Electrical and Computer Engineering of University of Missouri-Rolla (UMR) where he worked on printed circuit boards and finite-difference time-domain techniques. His research activity is mainly in the field of electromagnetic compatibility (EMC) and includes numerical and analytical techniques for modelling high-speed printed circuit boards, shielding, and transmission line analysis.

Dr. Araneo received the Past President's Memorial Award in 1999 from the IEEE Electromagnetic Compatibility Society. He is the present general chair of the IEEE International Conference on Environment and Electrical Engineering.



Paolo Burghignoli (S'97–M'01–SM'08) was born in Rome, Italy, on February 18, 1973. He received the Laurea degree (*cum laude*) in electronic engineering and Ph.D. degree in applied electromagnetics from the University of Rome “Sapienza”, Rome, Italy, in 1997 and 2001, respectively.

In 1997, he joined the Electronic Engineering Department, now the Department of Information Engineering, Electronics and Telecommunications, University of Rome “La Sapienza”, Rome, Italy, where, since November 2010, he has been an Assistant Professor. From January 2004 to July 2004, he was a Visiting Research Assistant Professor with the University of Houston, Houston, TX, USA. His scientific interests include analysis and design of planar antennas and arrays, leakage phenomena in uniform and periodic structures, numerical methods for integral equations and periodic structures, propagation and radiation in metamaterials,

ground-penetrating radars, scattering from moving objects, and electromagnetic shielding.

Dr. Burghignoli was the recipient of the “Giorgio Barzilai” Laurea Prize (1996–1997) presented by the former IEEE Central & South Italy Section, a 2003 IEEE Microwave Theory and Techniques Society (MTT-S) Graduate Fellowship, and a 2005 Raj Mittra Travel Grant for Junior Researchers presented at the IEEE Antennas and Propagation Society Symposium on Antennas and Propagation, Washington, DC, USA. He is a coauthor of the “Fast Breaking Papers, October 2007” in EE and CS, about metamaterials (paper that had the highest percentage increase in citations in Essential Science Indicators, ESI).



George W. Hanson (S'85–M'91–SM'98–F'09) was born in Glen Ridge, NJ, USA, in 1963. He received the B.S.E.E. degree from Lehigh University, Bethlehem, PA, USA, in 1986, the M.S.E.E. degree from Southern Methodist University, Dallas, TX, USA, in 1988, and the Ph.D. degree from Michigan State University, East Lansing, MI, USA, in 1991.

From 1986 to 1988, he was a Development Engineer with General Dynamics, Fort Worth, TX, USA, where he worked on radar simulators. From 1988 to 1991, he was a Research and Teaching Assistant with the Department of Electrical Engineering, Michigan State University. He is currently a Professor of electrical engineering and computer science with the University of Wisconsin-Milwaukee, Milwaukee, WI, USA. He is coauthor of the book *Operator Theory for Electromagnetics: An Introduction* (Springer, 2002) and author of *Fundamentals of Nanoelectronics* (Prentice-Hall, 2007). His research interests include nanoelectromagnetics, quantum optics, mathematical methods in electromagnetics, and electromagnetic wave phenomena in layered media.

Dr. Hanson is a member of URSI Commission B, Sigma Xi, and Eta Kappa Nu, and was an associate editor for the IEEE TRANSACTIONS ON ANTENNAS AND PROPAGATION from 2002 to 2007. In 2006, he was the recipient of the S.A. Schelkunoff Best Paper Award from the IEEE Antennas and Propagation Society.